The Comparative Study of Thermoelectric Properties in $Sb_2Si_2Te_6$ and $Bi_2Si_2Te_6$

Hanhwi Jang,[1] Abbey Stanley,[2] Brakowaa Frimpong,[2] Chien Viet Nguyen,[3] Pawel Ziolkowski[4], Gregor Oppitz[4], Moohyun Kim[1], Jae Yong Song,[3] Ho Sun Shin,[3] Yeon Sik Jung,[1] and Min-Wook Oh*[2]

[1]Department of Materials Science and Engineering, Korea Advanced Institute of Science and Technology (KAIST), Daejeon 34141, Republic of Korea

[2]Department of Materials Science and Engineering, Hanbat National University, Daejeon 34158, Republic of Korea

[3]Korea Research Institute of Standards and Science (KRISS), Daejeon 34113, Republic of Korea

[4]Institute of Materials Research, German Aerospace Center (DLR), Cologne 51147, Germany

KEYWORDS: Thermoelectrics; Heterointerfaces; Phase boundary scattering; Point defects; Thermal conductivity

ABSTRACT: The charge carrier transport and corresponding thermoelectric properties are often affected by several parameters, necessitating a thorough comparative study for a profound understanding of the detailed conduction mechanism. Here, as a model system, we compare the electronic transport properties of two layered semiconductors, $Sb_2Si_2Te_6$ and $Bi_2Si_2Te_6$. Both materials have similar grain sizes and morphologies, yet their conduction characteristics are significantly different. We found that phase-boundary scattering can be one of the main factors for in $Bi_2Si_2Te_6$ to experience significant charge carrier scattering whereas $Sb_2Si_2Te_6$ is relatively unaffected by the phenomenon. Furthermore, extensive point-defect scattering in $Sb_2Si_2Te_6$ significantly reduces its lattice thermal conductivity and results in high zT values across a broad temperature range. These findings provide novel insights into electron transport within these materials and should lead to strategies for further improving their thermoelectric performance.

1. Introduction

Recently, thermoelectric (TE) energy conversion technologies are attracting significant attention owing to the fact that the generation of electricity from conventional turbines results in undesirable CO_2 emissions as well as noise.[1-3] Nevertheless, the efficiency of TE generators is markedly lower than those of other energy-harvesting technologies, and their market growth has stagnated for years.[4] The ideal efficiency of TE materials can be determined using the dimensionless figure of merit $zT = S^2\sigma T/\kappa_{tot}$, where S, σ, T, and κ_{tot} are the Seebeck coefficient, electrical conductivity, absolute temperature, and total thermal conductivity of the TE material.[5, 6] It is well known that materials with high zT values exhibit high conversion efficiencies. However, increasing zT is challenging because the various material properties are highly interdependent.

Therefore, researchers have focused on developing novel TE materials with high performance, such as Bi_2Te_3[7-11], GeTe[12-16], PbTe[17-20], SnSe[21-24], $AgBiSe_2$[25-27], Mg_3Sb_2[3, 28, 29], half-Heuslers[30, 31], and metal silicides[32-36]. Among the various TE materials being explored, $Sb_2Si_2Te_6$ constitutes an emerging class of layered p-type TE materials.[37] Even when undoped, it has an intrinsically high hole concentration at $6 \times 10^{19}/cm^3$ yet shows a reasonably high Seebeck coefficient at 120 μV/K. Furthermore, its layered crystal structure and high Grüneisen parameter value result in exceptionally low lattice thermal conductivity (κ_{latt}). These intriguing features make $Sb_2Si_2Te_6$ suitable for use as a high-performance TE material.

The existence of its chemical family, $Bi_2Si_2Te_6$, has already been predicted by first-principles calculations. Similar to $Sb_2Si_2Te_6$, $Bi_2Si_2Te_6$ is expected to have a layered crystal structure but a slightly smaller bandgap compared with that of $Sb_2Si_2Te_6$.[38] In terms of thermal properties, $Bi_2Si_2Te_6$ is expected to exhibit a lower κ_{latt} value than that of $Sb_2Si_2Te_6$ owing to the substitution of Sb by the heavy Bi atoms, which may also result in high zT values. However, the electronic and thermal transport properties of polycrystalline $Bi_2Si_2Te_6$ have not been investigated experimentally. Therefore, we synthesized $Bi_2Si_2Te_6$ and evaluated its TE properties to elucidate the structure–property relationship for $Sb_2Si_2Te_6$ and $Bi_2Si_2Te_6$.

In this work, we report, for the first time, the TE properties of polycrystalline $Bi_2Si_2Te_6$ and compare them with those of $Sb_2Si_2Te_6$. Through systematic characterization measurements, we were able to elucidate the complex microstructures of $Sb_2Si_2Te_6$ and $Bi_2Si_2Te_6$ and evaluate the effects of their heterointerfaces. The electronic transport properties of $Sb_2Si_2Te_6$ are superior to those of $Bi_2Si_2Te_6$. This can be attributed to the suppression of phase-boundary scattering at the heterointerfaces in the former. Moreover, it was found that point-defect scattering is the principal mechanism responsible for the reduced lattice

thermal conductivity of $Sb_2Si_2Te_6$. These findings emphasize the importance of understanding the phenomenon of electron transport at interfaces with respect to the development of high-performance TE materials.

2. Results and discussion

2.1. Phase and structural characterization

The phase purities and crystal structures of the synthesized samples were characterized using powder X-ray diffraction (XRD) analysis. Figure 1c and 1d show the powder XRD patterns of $Sb_2Si_2Te_6$ and $Bi_2Si_2Te_6$, respectively. Both materials have a trigonal structure with space group *R-3*. In addition, all the diffraction peaks with the except of that at approximately θ = 42° could be indexed to either $Sb_2Si_2Te_6$ or $Bi_2Si_2Te_6$. We found that this extra peak arises from the Sb_2Te_3 and Bi_2Te_3 secondary phases. The results of a quantitative analysis indicated that the volume fractions of Sb_2Te_3 and Bi_2Te_3 in the matrix were 22.9% and 9.32% for $Sb_2Si_2Te_6$ and $Bi_2Te_2Te_6$, respectively. Although we used the synthesis procedures reported by Luo et al., the volume fractions of the secondary phases were greater than reported values by Luo et al. (0.6 wt%).[37] Moreover, the difference in the phase purities was probably related to the differences in the processing conditions such as the ball-to-powder ratio, volume of the jar used, and annealing environment.

The presence of secondary phases was also confirmed by transmission electron microscopy (TEM) imaging. The high-angle annular dark-field scanning TEM (HAADF-STEM) images and corresponding elemental mapping by energy dispersive X-ray spectroscopy (EDS) in Figure 1a and 1b show that large Sb-Te-or Bi-Te-rich precipitates as well as Si and Te nanoprecipitates were present in the samples. The lateral size of the Sb-Te precipitates was as high as a few micrometers, which is almost double that of the Bi-Te precipitates. This is consistent with results of the XRD analysis, which suggested that the amount of Sb_2Te_3 was nearly twice that of Bi_2Te_3. Moreover, although Si and Te nanoprecipitates were also present, their contents were extremely low since related peaks could not be observed in the XRD patterns. Table 1 lists the experimentally measured lattice parameters of $Sb_2Si_2Te_6$ and $Bi_2Si_2Te_6$ and compares them with those determined by density functional theory (DFT) calculations.[38] The measured value for $Sb_2Si_2Te_6$ is almost identical to that reported previously.[37] Moreover, the lattice parameter of $Bi_2Si_2Te_6$ was slightly higher compared with that of $Sb_2Si_2Te_6$. This is because the ionic radius of Bi^{3+} (103 pm) is larger than that of Sb^{3+} (76 pm).[39] Note that the lattice parameters as obtained from the DFT calculations may be overestimated when the generalized gradient approximation (GGA) exchange-correlation functional is implemented.[40 41]

2.2. Electronic transport properties

$Sb_2Si_2Te_6$ exhibits superior electronic transport properties compared with those of $Bi_2Si_2Te_6$. Figure 2a and 2b show the temperature-dependent Seebeck coefficient (S) and the electrical conductivity (σ) of both materials. The S value of $Sb_2Si_2Te_6$ increased with increasing temperature, indicating that $Sb_2Si_2Te_6$ shows degenerate conduction characteristics. Similarly, the S value of $Bi_2Si_2Te_6$ increased till approximately 550 K and then decreased monotonically till 773 K. In addition, the Seebeck coefficients of $Sb_2Si_2Te_6$ and $Bi_2Si_2Te_6$ were positive, implying that for both materials, the conduction process is primarily governed by holes. The σ value of $Bi_2Si_2Te_6$ increased with increasing temperature, starting at 673 K, suggesting that $Bi_2Si_2Te_6$ shows nondegenerate conduction characteristics. The n-like shape of the curve for the Seebeck coefficient can be attributed to bipolar conduction, which can be expressed using the following equation:

$$S = \frac{S_p\sigma_p - S_n\sigma_n}{\sigma_p + \sigma_n},$$

where S_p, S_n, σ_p, and σ_n are the Seebeck coefficients of holes and electrons, and the electrical conductivities of holes and electrons, respectively.[42] When the electron concentration is comparable to that of holes owing to thermal excitation, the magnitude of the Seebeck coefficient decreases because S_n compensates S_p.

It is known that TE properties of materials significantly vary due to several factors such as the electronic band structure, band gap, and even the spatial distribution and molar fraction of the secondary phases. Therefore, the aforementioned factors should be considered to understand the complex TE properties of the current samples. As both $Sb_2Si_2Te_6$ and $Bi_2Si_2Te_6$ exhibit a peak Seebeck coefficient at a certain temperature, their electronic bandgaps can be estimated using the Goldsmid–Sharp rule, which is given by the following equation:

$$E_{g,GS} = 2|S_{max}|T_{max},$$

where S_{max} is the maximum Seebeck coefficient and T_{max} is the temperature corresponding to S_{max}.[43, 44] The bandgap calculated using the Goldsmid–Sharp rule was 0.33 eV for $Sb_2Si_2Te_6$ and 0.21 eV for $Bi_2Si_2Te_6$. The calculated bandgap of 0.33 eV for $Sb_2Si_2Te_6$ is almost half of that reported by Luo et al. (optical bandgap of 0.6 eV).[37] Therefore, we measured the optical absorption spectra of $Sb_2Si_2Te_6$ and $Bi_2Si_2Te_6$ and determined their optical bandgaps, which were found to be 0.4 eV and 0.28 eV, respectively (Figure S1). Furthermore, the DFT-calculated bandgaps of $Sb_2Si_2Te_6$ and $Bi_2Si_2Te_6$ are 0.15 eV and 0.07 eV, respectively.[38] These results confirm that both materials have a narrow bandgap, which ranges from 0.2 to 0.4 eV. This is consistent with the electronic property measurement results, according to which $Bi_2Si_2Te_6$ exhibits bipolar conduction while $Sb_2Si_2Te_6$ does not.

We found that $Sb_2Si_2Te_6$ is also resistant to carrier scattering at the phase boundaries. Figure 2c shows the calculated weighted mobilities (μ_w) of $Sb_2Si_2Te_6$ and $Bi_2Si_2Te_6$. Similar to the Hall mobility, the temperature-dependent μ_w can be used to understand the charge-transport mechanism.[45] One can see that in the case of $Sb_2Si_2Te_6$, μ_w is dependent on $T^{-1.5}$, suggesting that electron–phonon scattering (or deformation potential scattering) is the predominant scattering mechanism.[46, 47] However, the μ_w value of $Bi_2Si_2Te_6$ is not dependent on $T^{-1.5}$ for temperatures close to room temperature and those higher than 600 K. As discussed above, $Bi_2Si_2Te_6$ exhibits strong bipolar conduction at temperatures higher than 600 K owing to its small bandgap. Hence, the reason for the observed deviation at high temperatures is the bipolar effect of electrons and holes. Interestingly, at temperatures close to room temperature, μ_w increased with increasing temperature. This behavior has also been observed in Mg_3Sb_2-based systems when a higher degree of grain-boundary scattering hinders electron transport.[47, 48] The positive slope of μ_w can be attributed to the thermal activation of charge carriers, which helps overcome scattering in

certain media.[49] However, in contrast to previous studies, we did not observe a significant difference in the grain morphologies of $Sb_2Si_2Te_6$ and $Bi_2Si_2Te_6$ (Figure 2d and 2e). This is reasonable as both materials were synthesized and sintered under the same conditions. Hence, we suspect that the observed precipitates act as a phase boundary, resulting in a strong scattering effect similar to that of grain-boundary scattering. In the next section, we propose an explanation why phase-boundary scattering has no effect on the electronic transport properties of $Sb_2Si_2Te_6$.

2.3. Thermal properties and compositional analysis

It is known that $Sb_2Si_2Te_6$ exhibits ultralow thermal conductivity (κ) owing to its high Grüneisen parameter values and low phonon group velocity.[37] We expected that $Bi_2Si_2Te_6$ could exhibit an even lower κ value than $Sb_2Si_2Te_6$ because the atomic number (Z) of Bi is larger than for Sb.[50] However, both the total thermal conductivity (κ_{tot}) and lattice thermal conductivity (κ_{latt}) of $Sb_2Si_2Te_6$ were significantly lower than those of $Bi_2Si_2Te_6$ (Figure 3a and 3b). The κ_{latt} value of $Bi_2Si_2Te_6$ decreases from 0.85 W $m^{-1}K^{-1}$ at 323 K to 0.60 $Wm^{-1}K^{-1}$ at 773 K. Similarly, the κ_{latt} value of $Sb_2Si_2Te_6$ drops from 0.72 W $m^{-1}K^{-1}$ at 323 K to 0.26 $Wm^{-1}K^{-1}$ at 773 K. The κ_{latt} value of our sample is almost 30% lower than that reported by Luo et al. at temperatures close to room temperature.[37] We attribute this reduction in κ_{latt} to the presence of nano- and micro-sized precipitates shown in Figure 1. These micro-sized precipitates effectively scatter long-wavelength phonons at temperatures close to room temperature while the nano-sized precipitates consistently scatter short-wavelength phonons over the entire temperature range.[19]

The observed low κ_{latt} value of $Sb_2Si_2Te_6$ can be explained by the results of the STEM-EDS compositional analysis and Hall measurements. As shown in Figure 3c and 3d, the $Sb_2Si_2Te_6$ and $Bi_2Si_2Te_6$ matrices are Si- and Te-deficient. This may be owing to the precipitated Si and Te secondary phases observed during XRD and STEM analyses. Luo et al. reported that Sb vacancies (V_{Sb}) are the reason for the high hole concentration of $Sb_2Si_2Te_6$ because V_{Sb} has the lowest DFT-calculated formation energy among all possible point defects.[37] However, it is also likely that Si vacancies act as acceptors to increase the hole concentration as the matrix is Si-deficient. Interestingly, the measured hole concentration of $Sb_2Si_2Te_6$ was 10 times greater than that of $Bi_2Si_2Te_6$, although their constituent element ratios were similar. This implies that the formation energy of V_{Sb} is lower than that of V_{Bi} yielding the high concentration of point defects in $Sb_2Si_2Te_6$. Thus, point defects in $Sb_2Si_2Te_6$ can effectively scatter short-wavelength phonons and reduce the value of κ_{latt} at high temperatures. Indeed, the κ_{latt} value of $Sb_2Si_2Te_6$ is 15.2% lower than that of $Bi_2Si_2Te_6$ at 323 K but 56.6% lower at 773 K.

The intrinsic thermal properties of materials are mainly determined by the Grüneisen parameter, which is a degree of anharmonicity present in the phonon dispersion. The estimated Grüneisen parameters of $Sb_2Si_2Te_6$ and $Bi_2Si_2Te_6$, which have been deduced from the elastic properties, were 2.98 and 2.53, respectively (Table S3). The larger Grüneisen parameter of $Sb_2Si_2Te_6$ would lead to the much low κ_{latt} determined by Umklapp process. However, a theoretical calculation based on the modified Debye–Callaway model overestimates the lattice thermal conductivity of both materials if the Umklapp process is considered only (Figure S7). Thus, it can be inferred that the principal reason for lower κ_{latt} values of $Sb_2Si_2Te_6$ than that of $Bi_2Si_2Te_6$ would mainly originate from the high Grüneisen parameter, as well as a combined effect of the strong point-defect scattering, and phase boundary scattering. Based on the EDS quantification results, we could evaluate the transport characteristics of the secondary phase in $Bi_2Si_2Te_6$. As the $Bi_2Si_2Te_6$ matrix is Bi-rich, its precipitate (Bi_2Te_3) would be Bi-poor. As a result, Bi_2Te_3 exhibits n-type conduction because of the Te_{Bi} antisite defects.[51, 52] Therefore, n-type Bi_2Te_3 precipitates form a highly resistive phase boundary within the p-type $Bi_2Si_2Te_6$ matrix. Similarly, the Sb_2Te_3 precipitates in $Sb_2Si_2Te_6$ are Sb-poor. However, Sb_2Te_3 always exhibits p-type conduction because of the significantly low formation energy of Sb_{Te}.[52, 53] As a result, the phase boundary between $Sb_2Si_2Te_6$ and Sb_2Te_3 is less resistive to holes than that between $Bi_2Si_2Te_6$ and Bi_2Te_3.

2.4. Mechanism responsible for high zT of $Sb_2Si_2Te_6$

The systematic investigations described above suggested that (i) the phenomena of strong phase-boundary scattering and (ii) significant point-defect scattering are responsible for the high zT values of $Sb_2Si_2Te_6$, as described in Figure 4a. Even though the volume fraction of the secondary phase of $Sb_2Si_2Te_6$ is approximately three times that of $Bi_2Si_2Te_6$, the former exhibits superior electronic transport properties owing to its homogeneous p-type phase boundary. However, $Bi_2Si_2Te_6$ experiences significant phase-boundary scattering at temperatures close to room temperature because of its resistive, n-type phase boundary (Figure 4b). This fact is further corroborated by transient potential Seebeck microscopy (T-PSM) measurements (Figure 4c and 4d). The spatial distribution of the Seebeck coefficient was uniformly p-type for $Sb_2Si_2Te_6$. However, $Bi_2Si_2Te_6$ shows distinctive p- and n-type regions, which consists of p-type matrix and n-type Bi_2Te_3 precipitates.

The above characteristics can be reasonably understood by the valence band offset (ΔE_{VB}), which acts as a barrier to hole transport. The ionization energy (IE) of $Sb_2Si_2Te_6$ as measured by ultraviolet photoelectron spectroscopy (UPS) was 4.78 eV, which is consistent with the previous result of Luo et al. (Figure S4).[37] It is known that the IE of Sb_2Te_3 is 4.45 eV, yielding ΔE_{VB} of 0.33 eV.[54] However, given that the Fermi level of $Sb_2Si_2Te_6$ lies 0.26 eV above that of Sb_2Te_3, the effective ΔE_{VB} would be 0.07 eV after Fermi level alignment (Figure S5). The measured IE value of $Bi_2Si_2Te_6$ was 4.85 eV, giving an ΔE_{VB} value of 0.52 eV. However, this energy barrier does not decrease significantly after Fermi level alignment, and the effective ΔE_{VB} is approximately 0.37 eV, almost 5 times to that of the $Sb_2Si_2Te_6$–Sb_2Te_3 system. From this estimation of ΔE_{VB}, we can infer that the principal mechanism for the severe phase boundary scattering of $Bi_2Si_2Te_6$ stems from the misalignment of the valence band maximum. Similar observations have been made in various TE systems, where a small variation in ΔE_{VB} between the matrix and secondary phase dramatically changes the electronic transport properties.[55-59] In addition, it is noteworthy that endotaxial nanostructures, i.e., secondary phases with a coherent interface to the matrix, can minimize the detrimental effects on carrier mobility.[55, 56, 59] Hence, crystal coherency between the matrix and secondary phases could affect the overall electronic transport properties in $Sb_2Si_2Te_6$ and $Bi_2Si_2Te_6$.

We quantitatively evaluated the electronic transport properties of $Sb_2Si_2Te_6$ based on the electronic quality factor (B_e).[60]

As can be seen from Figure 4e and 4f, the fitted B_e value of $Sb_2Si_2Te_6$ is 1.8, which is slightly lower than that reported by Luo et al. ($B_e = 2.6$). This difference can be attributed to the scattering of holes in the secondary phases. However, one should also consider that the κ_{latt} value of our sample is almost 30% lower than that reported by Luo et al. This eventually yields a similar thermoelectric quality factor ($B \propto B_e T/\kappa_{latt}$). However, $Bi_2Si_2Te_6$ exhibits a maximum B_e of 0.7, and its B_e value is lower at temperatures close to room temperature as well as at high temperatures owing to additional scattering mechanisms. With its low B_e value, its relatively high κ_{latt} results in significantly lower zT values over both low- and high-temperature range. As illustrated above, a frequent scattering of charge carriers in $Bi_2Si_2Te_6$ results from several scattering centers: bipolar transport from narrow band gap and resistive phase boundary formed by Bi_2Te_3. This leads to the relatively small power factor and corresponding low B_e value. Moreover, the modest concentration of point defects and smaller Grüneisen parameter of $Bi_2Si_2Te_6$ compared to that of $Sb_2Si_2Te_6$ result in high κ_{latt} values. The calculated zT values in Figure 4f clearly highlight the detrimental effect of phase-boundary scattering in $Bi_2Si_2Te_6$ as well as that of its bipolar conduction characteristics. In contrast, $Sb_2Si_2Te_6$ exhibits a high zT value (>1) owing to the point-defect scattering of phonons but does not show significant bipolar scattering.

3. Conclusions

In summary, we successfully synthesized $Sb_2Si_2Te_6$ and $Bi_2Si_2Te_6$ by a solid-state reaction method and measured the TE properties of polycrystalline $Bi_2Si_2Te_6$ for the first time. We found that both, $Sb_2Si_2Te_6$ and $Bi_2Si_2Te_6$ contain several types of nanoscale precipitates within their matrices. However, these have an opposite effect on the electronic transport properties of both materials. Similar to the case for other high-performance TE materials, in $Sb_2Si_2Te_6$, hole carriers are mainly scattered because of electron–phonon scattering. However, $Bi_2Si_2Te_6$ experiences significant phase-boundary scattering and bipolar transport over nearly all operating temperature ranges and exhibits low zT values. Furthermore, we found that point-defect scattering plays a critical role in ensuring that the lattice thermal conductivity of $Sb_2Si_2Te_6$ is low. On the other hand, the formation of point defects is inhibited in $Bi_2Si_2Te_6$. The results of this work not only highlight the importance of understanding the fundamental scattering mechanism in TE materials but can also serve as guidelines for further improvement of the performance of other TE materials through interface engineering.

4. Experimental section

Reagents: Sb shots (99.999%, 5N Plus), Bi shots (99.999%, 5N Plus), Te shots (99.999%, 5N Plus), and Si granules (99.999%, 5N Plus) were used as received without further purification.

Synthesis: We synthesized $Sb_2Si_2Te_6$ and $Bi_2Si_2Te_6$ by ball milling and annealing as per the method described by Luo et al.[37] Stoichiometric amounts of the starting materials were added to a zirconia jar (70 mL) along with zirconia balls (diameter of 10 mm). The ball-to-powder ratio was 10:1. To prevent oxidation during the milling process, the jar was evacuated, filled with N_2 gas, and sealed. The milling process was performed using a planetary ball mill (Pulverisette 7, Fritsch) at 450 rpm for 2 h. The obtained powder was pressed into a pellet using a hydraulic press under a uniaxial pressure of 200 MPa. The obtained pellet was placed in a tube furnace under a constant Ar gas flow (190 mL/min). The tube furnace was heated to 823 K for 2 h, annealed at this temperature for 48 h, and cooled to room temperature.

Densification: The obtained sample was ground into a powder using an agate mortar and placed in a graphite mold (diameter of 12.7 mm). Graphite punches of the same diameter were used during the densification process. The powder was densified by spark plasma sintering (Dr. SINTER SPS-211Lx, Fuji Electronic Industrial) in vacuum at 773 K for 10 min under a uniaxial pressure of 50 MPa.

Measurement of TE properties: The obtained sample was machined into a rectangular bar (3×3×8 mm^3) and a cylinder (Φ12.7×1 mm^3), which were used to measure the electrical and thermal properties, respectively. S and σ were measured simultaneously using a commercial apparatus (BS-1, Bluesys) with a four-probe setup under a weak He backpressure to minimize sample outgassing and improve the contact between the sample and the measuring electrodes. The temperature gradient between the heater electrode and heat sink electrode was set to 10, 20, and 30 K, and the actual temperature gradient across the sample was approximately 2 to 10 K. Before the measurements, we calibrated the equipment by using constantan as a reference material and performing measurements from 323 K to 773 K. We could confirm that the measured values lay within the standard error range of the S and σ values reported in the literature. The value of κ was calculated using the expression $\kappa = \rho \cdot C_p \cdot D$, where ρ is the bulk density, C_p is the specific heat capacity, and D is the thermal diffusivity. The value of ρ was measured by the Archimedes method, while C_p was calculated using the Dulong–Petit law. D was measured using a laser flash apparatus (LFA 457, Netzsch) in an Ar atmosphere. A thin graphite layer was coated on the sample surface to minimize sample evaporation and improve the emissivity of the sample. A pulse-corrected Cowan model was employed to calculate the D values.

XRD analysis: The XRD measurements were performed using an X-ray diffractometer (Smartlab, Rigaku) with a Cu-Kα radiation source and a Ge(111) monochromator. Whole-powder pattern fitting (WPPF) was performed using the software PDXL2 (Rigaku). The diffraction planes and corresponding Bragg angles were calculated using the software VESTA.

SEM analysis: Fracture surface analysis was performed using a field-emission scanning electron microscopy (SEM) system (S-4800, Hitachi) at an acceleration voltage of 20 kV.

TEM analysis: Thin lamellae samples for the TEM analysis were prepared with a focused ion beam system (Helios G4, FEI) using liquid Ga metal as the ion source. HAADF-STEM imaging and EDS elemental mapping were performed using a TEM system (Talos F200X, FEI) equipped with a Super X EDS detector.

Measurement of optical properties: The optical absorption spectra of the samples were acquired using a Fourier transform infrared spectrometer (Nicolet iS50, Thermo Scientific). Their optical reflectances were measured by diffuse reflectance spectroscopy, and their absorption coefficients were calculated using the Kubelka–Munk equation. The optical bandgap was obtained by the linear interpolation of the absorption spectrum from the Tauc plot.

Hall measurements: The Hall coefficient was measured using a Hall effect measurement system (HMS-3000, Ecopia) with the van der Pauw configuration at room temperature. The carrier concentration was calculated from the Hall coefficient. The high-temperature Hall measurements were conducted using a high-temperature apparatus (HMS 8407, Lake Shore Cryotronics) under a magnetic field of 1 T.

UPS measurements: Ultraviolet photoelectron spectroscopy (UPS) was conducted using electron spectroscopy for chemical analysis (ESCA) apparatus (Axis Supra, Kratos) with a He I radiation source (photon energy = 21.2 eV) in an ultra-high vacuum chamber (base pressure < 5×10^{-10} Torr). The sample spectra were calibrated using a gold (Au) standard sample stored in the load lock chamber.

Kelvin probe force microscopy (KPFM): We utilized KPFM measurements to analyze the spatial distribution of the work function. This method has been exploited in various materials systems including metals, ceramics, and conducting polymers.[61-63] Topographic image and contact potential difference (CPD) values were simultaneously obtained using an atomic force microscope (AFM; NX10, Park Systems) and Au-coated cantilevers (PPP-NCSTAu, Nanosensors). We used noncontact mode for topographic imaging and CPD measurements with a tip resonance frequency of 157 kHz and vibration amplitude of 21.98 nm. The typical setpoint and scan speed were 9.5 nm and 0.5 Hz, respectively. For CPD measurements, an AC voltage of 5 V with 17 kHz frequency was applied to the tip, and the response signals were acquired using a lock-in amplifier integrated in the AFM. The work function of the tip (φ_{tip}) was determined using a highly oriented pyrolytic graphite (HOPG) standard sample. Then, the sample work function (φ_s) was determined by the following equation: $\varphi_s = \varphi_{tip} - qV_{CPD}$, where q is the charge of an electron and V_{CPD} is the contact potential difference.[64]

Measurement of sound velocity: The sound velocity of $Sb_2Si_2Te_6$ and $Bi_2Si_2Te_6$ was measured by pulse-echo method, where a transducer first sends an initial pulse and acts as a receiver. A longitudinal transducer with a center frequency of 5 MHz (CMR-052, ndtXducer) and a normal incidence shear transducer of identical frequency (SM-052, ndtXducer) were used with an ultrasonic pulser/receiver system (DPR 300, JSR Ultrasonics). A resulting waveform was recorded by a digital oscilloscope (DSO-X 2022A, Keysight). The time delay of ultrasound reflections was determined by measuring time intervals between back wall echoes. Then, the speed of sound was calculated by the following equation: $v=2h/t$, where h is the sample thickness and t is the time delay.

Potential Seebeck microscope measurements: The Seebeck coefficient microprobe scanning was performed at room temperature and under vacuum on $Sb_2Si_2Te_6$ and $Bi_2Si_2Te_6$ samples using the transient Potential-Seebeck Microprobe (T-PSM). During the T-PSM measurement the sample surface is scanned by a heated tungsten carbide tip with a radius of curvature of 12 µm. The tip carries a laser-welded type-T thermocouple and builds the apex of a fiber optical cable. The optical cable is connected to a laser module (VFM 1,5-25, Messtec Power Converter GmbH), which delivers a maximum pulse energy of 1600 mW at a wavelength of 450 nm for thermal excitation of an infinitesimal sample volume. The laser diode (OSRAM PLTB450B built into Thorlabs collimation kit) was operated in a constant mode with a continuous beam power of 300 mW for the measurements. The sample was mounted within a sample holder on an encoder-controlled x-/y-motion stage from Micos (type: LS-110 52 VSS43 HV LIA) with a nanometer resolution. Another thermocouple of the same kind is attached to the sample holder, which is kept at room temperature during scanning by a passive heat sink. Once the tip contacts the sample surface, both thermocouples form two independent thermoelectric measurement circuits, which are fed to differential pre-amplifiers from Elsys Instruments (EL-LNA2) with high gain/bandwidth (100/5 MHz), low input noise (< $6\mu V_{rms}$) and electric isolation between input channels. The amplifier outputs are connected to a TransCom transient recorder (MF-Instruments) with a high sampling rate (max. 80 MHz/channel). A vertical z-axis actuator sets a reproducible tip pressure by a control loop with a force sensor from ALTHEN GmbH (type: 31E-001N5-30b), which ensures the necessitated high repeatability of thermal contact resistance between the tip and the sample surface. Measurement of the spatially resolved Seebeck coefficient is accomplished by a laser-based excitation of a local temperature gradient in a microscopic sample volume in the vicinity of the tip. The underlying evaluation of generated thermovoltages is described in the previous work.[65] The uncertainty of the measured Seebeck coefficient < 10%, which was determined against a reference value of $FeSi_2$ bulk reference material[66] with a certified uncertainty of the homogeneity of 2.4 µV/K, which corresponds to 1.4% of the expectation value at room temperature. The ability to resolve differences in thermopower remains unaffected from the absolute accuracy, yielding distinguishable Seebeck contrasts around 1-2% within the limits of local resolution.[67] While the predecessor PSM offered a lateral resolution of maximal 10 µm, the T-PSM resolves the local Seebeck coefficient on a length scale of 1-3 µm by a fast data acquisition during the transient process of laser-induced thermal excitation of the sample volume.

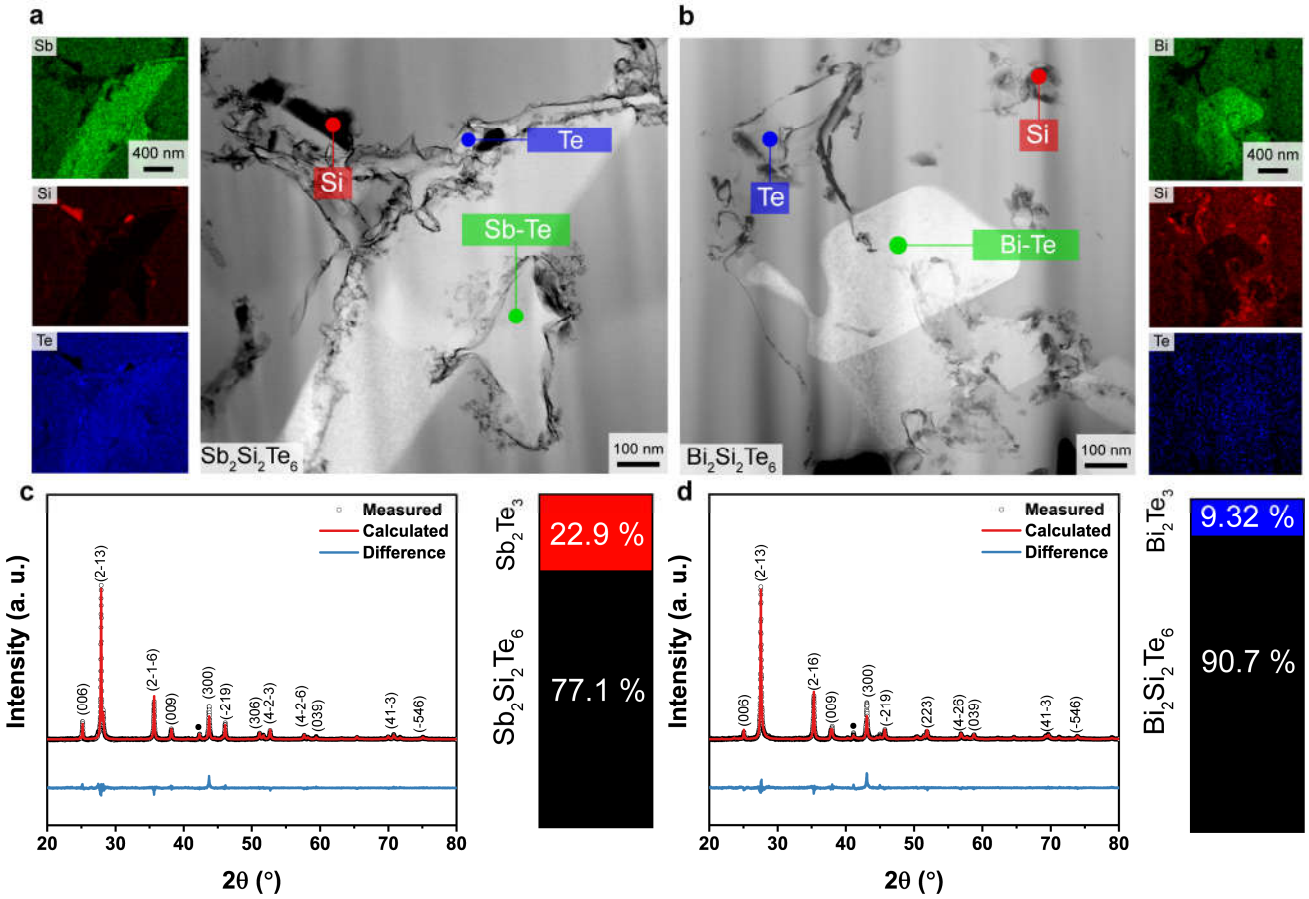

Figure 1. (a-b) HAADF-STEM images and corresponding EDS elemental maps of (a) $Sb_2Si_2Te_6$ and (b) $Bi_2Si_2Te_6$ indicating existence of several types of precipitates within matrix. (c-d) Refined powder XRD patterns and weight fractions of (c) $Sb_2Si_2Te_6$ and (d) $Bi_2Si_2Te_6$. Circles denote reflections from secondary phases (Sb_2Te_3 and Bi_2Te_3).

Table 1. DFT-calculated lattice parameters of $Sb_2Si_2Te_6$ and $Bi_2Si_2Te_6$ and experimentally measured values obtained after Rietveld refinement

Composition	a (calc/Å)	a (exp/Å)	c (calc/Å)	c (exp/Å)
$Sb_2Si_2Te_6$	7.223	7.166	21.236	21.205
$Bi_2Si_2Te_6$	7.316	7.270	21.438	21.311

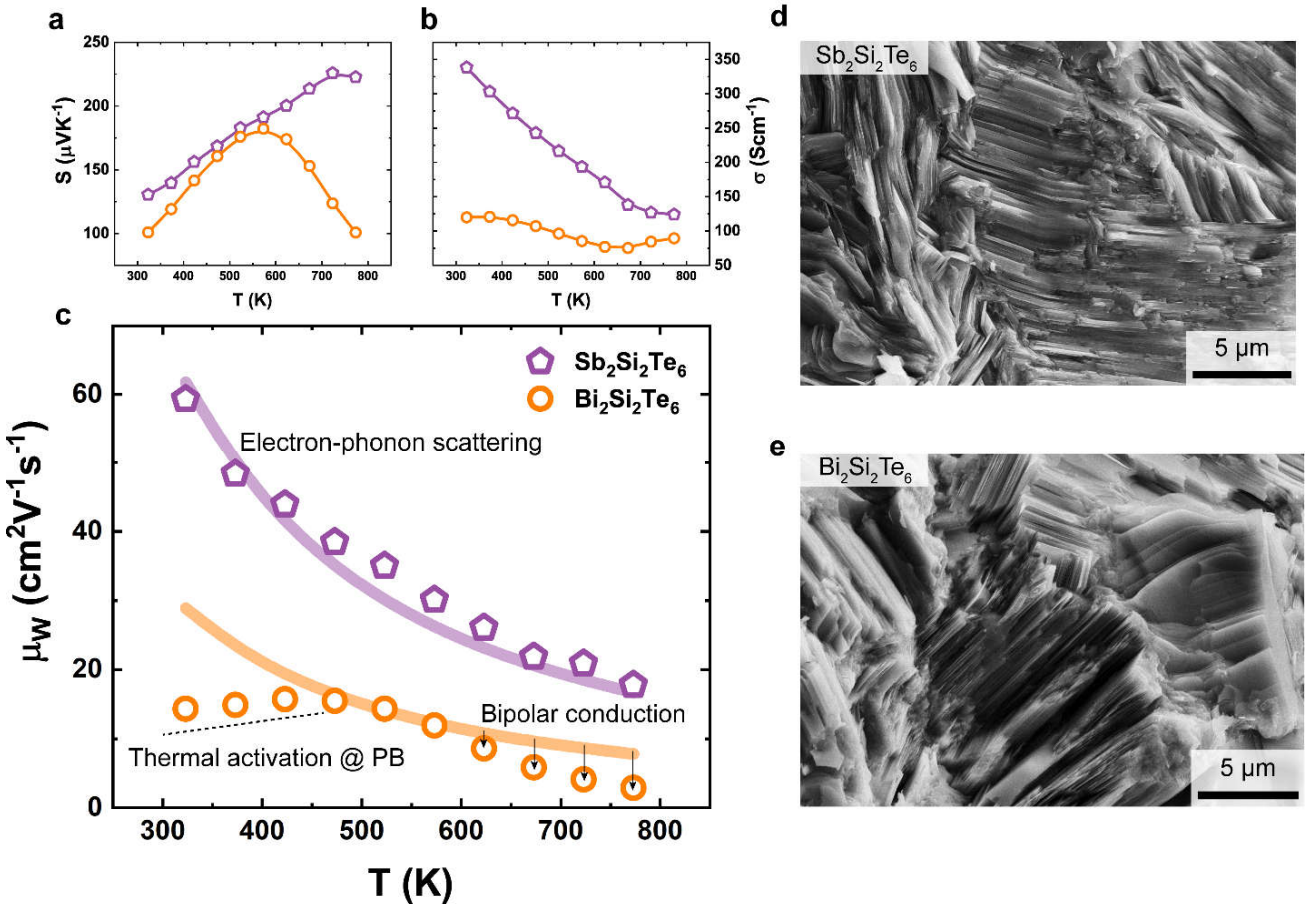

Figure 2. (a) Seebeck coefficient (S), (b) electrical conductivity (σ), and (c) weighted mobility (μ_w) values of $Sb_2Si_2Te_6$ and $Bi_2Si_2Te_6$. Solid lines in (c) show $T^{-1.5}$ dependence of μ_w where electron–phonon scattering is the predominant mechanism of hole transport. (d-e) Typical SEM images of fracture surfaces of (d) $Sb_2Si_2Te_6$ and (e) $Bi_2Si_2Te_6$ samples. Both samples show similar layered crystal structure and lateral grain size of approximately 20 μm.

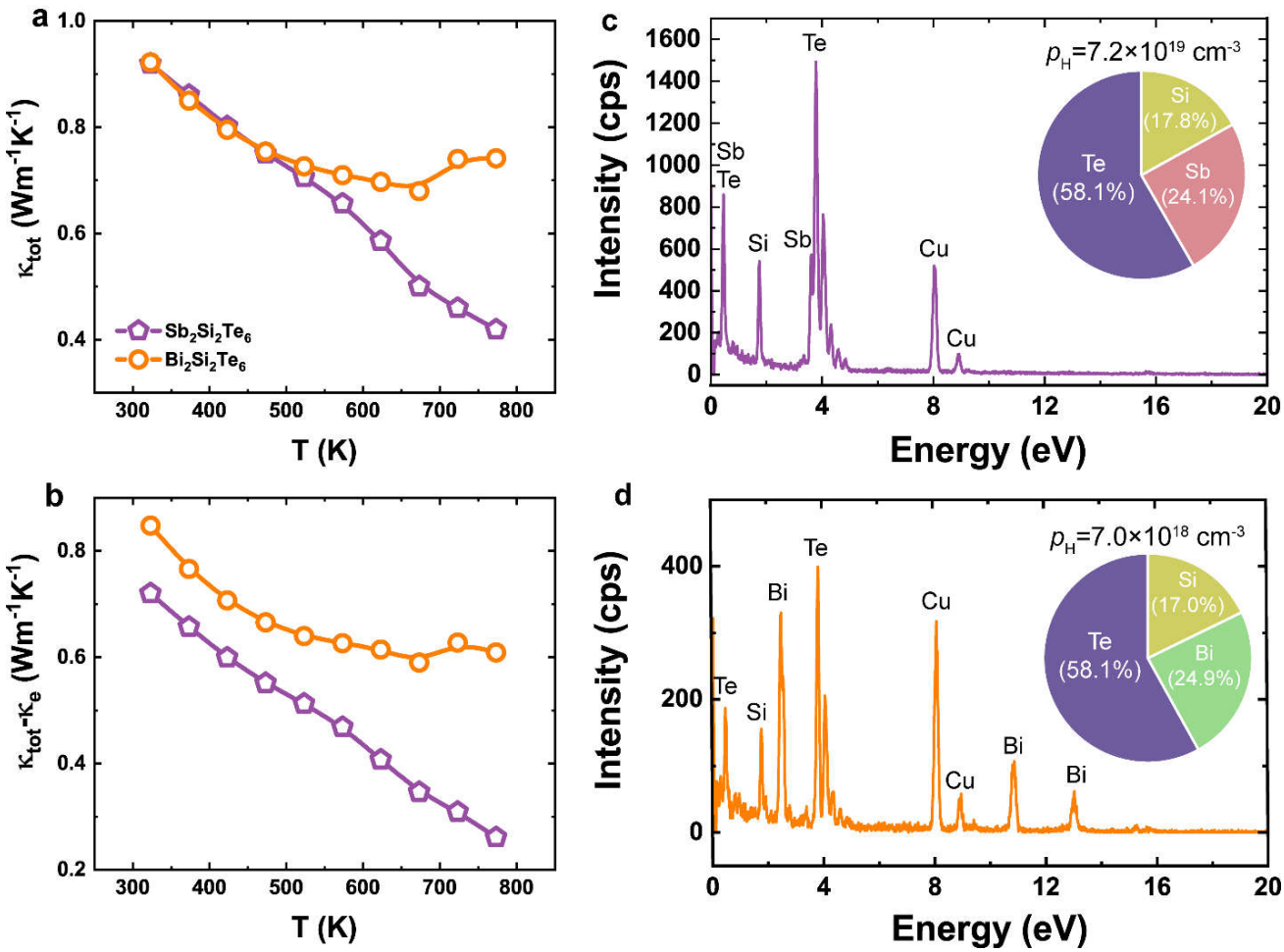

Figure 3. (a) Total thermal conductivity (κ_{tot}) and (b) lattice and bipolar components (κ_{tot}- κ_e) of $Sb_2Si_2Te_6$ and $Bi_2Si_2Te_6$. (c-d) STEM-EDS spectra and corresponding elemental components of (c) $Sb_2Si_2Te_6$ and (d) $Bi_2Si_2Te_6$ matrices along with measured Hall carrier concentrations. Cu peaks correspond to TEM grid.

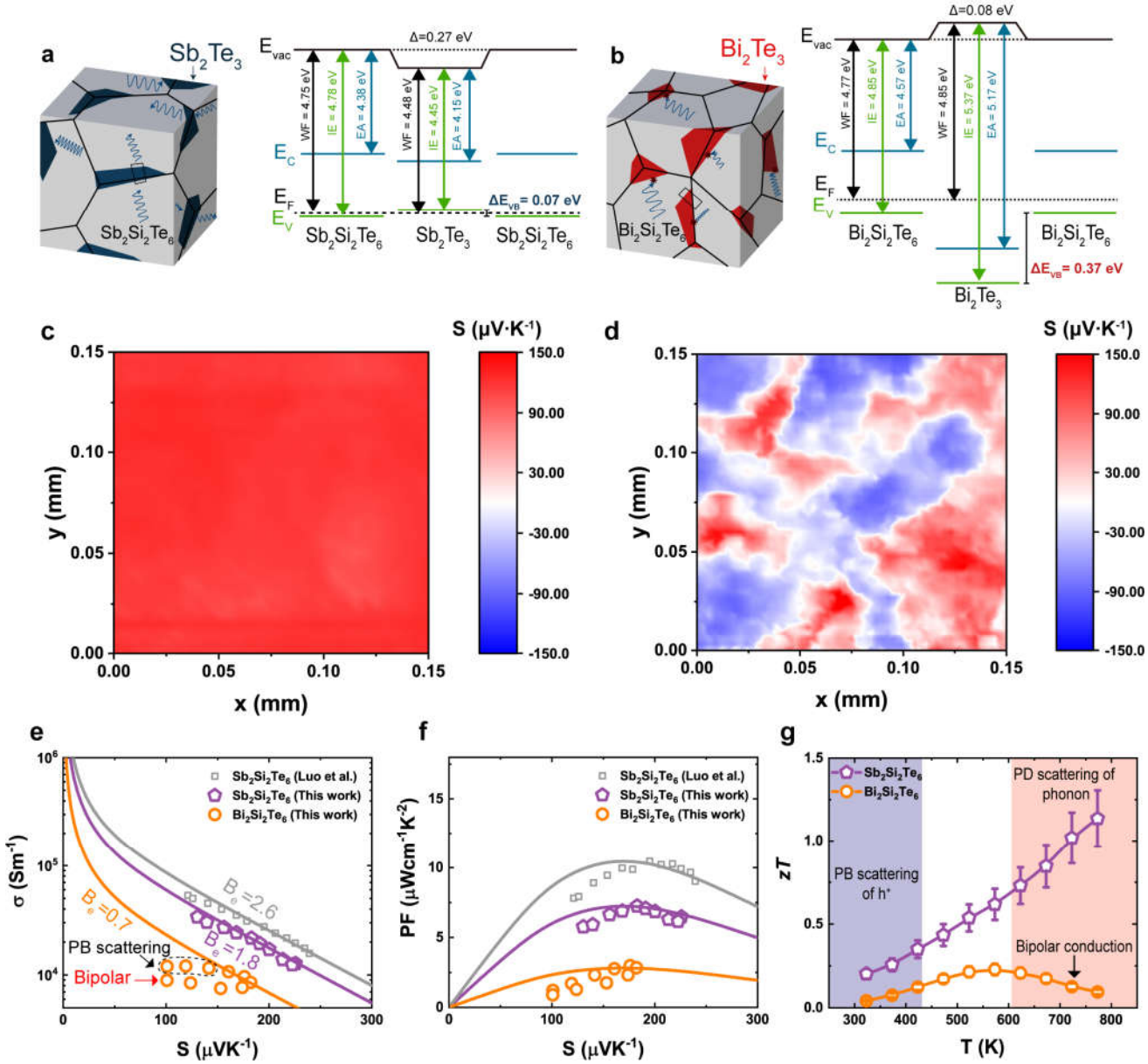

Figure 4. (a-b) Schematic drawing of hole transport and corresponding energy level diagram in (a) $Sb_2Si_2Te_6$ and (b) $Bi_2Si_2Te_6$ near precipitates. (c-d) Spatial distribution of Seebeck coefficient for (c) $Sb_2Si_2Te_6$ and (d) $Bi_2Si_2Te_6$. Negative Seebeck coefficient in (d) emerges from Bi_2Te_3 precipitates. (e-f) Curves of Seebeck coefficient (S)-dependent (e) electrical conductivity (σ) and (f) power factor (PF) fitted using certain electronic quality factor (B_e). (g) Temperature-dependent dimensionless figures of merit (zT) of $Sb_2Si_2Te_6$ and $Bi_2Si_2Te_6$.

ASSOCIATED CONTENT

Supporting Information. Optical absorption spectra of $Sb_2Si_2Te_6$ and $Bi_2Si_2Te_6$, additional EDX elemental mappings of $Sb_2Si_2Te_6$ and $Bi_2Si_2Te_6$, summary of UPS measurements, KPFM results, high-temperature Hall measurements, and characterization of samples annealed for 240 h.

AUTHOR INFORMATION

Corresponding Author

Min-Wook Oh – Department of Materials Science and Engineering, Hanbat National University, Daejeon 34158, Republic of Korea; Email: mwoh@hanbat.ac.kr

Author Contributions

H. Jang and M.-W. Oh conceived the idea. H. Jang, A. Stanley, and B. Frimpong synthesized and characterized the materials. H. Jang, C. V. Nguyen, J. Y. Song, and H. S. Shin densified the powders into pellets. H. Jang and M. Kim measured KPFM. P. Ziolkowski and G. Oppitz measured the spatial distribution of Seebeck coefficient using T-PSM. H. Jang wrote the manuscript from all input of the authors. Y. S. Jung and M.-W. Oh supervised the work.

Notes

The authors declare no competing financial interest.

ACKNOWLEDGMENT

This work was supported by the Creative Materials Discovery Program through the National Research Foundation of the Republic of Korea (NRF) funded by Ministry of Science and ICT (No. 2020M3D1A1070053) and International Energy Joint R&D Program of the Korea Institute of Energy Technology Evaluation and Planning (KETEP) granted from the Ministry of Trade, Industry & Energy (MOTIE), Republic of Korea (No. 20188550000290)

REFERENCES

1. Snyder, G. J.; Toberer, E. S., Complex thermoelectric materials. *Nat. Mater.* **2008,** *7* (2), 105-114.
2. Mao, J.; Chen, G.; Ren, Z., Thermoelectric cooling materials. *Nat. Mater.* **2020**. *20* (4), 454-461.
3. Mao, J.; Zhu, H.; Ding, Z.; Liu, Z.; Gamage, G. A.; Chen, G.; Ren, Z., High thermoelectric cooling performance of n-type Mg3Bi2-based materials. *Science* **2019,** *365* (6452), 495-498.
4. He, J.; Tritt, T. M., Advances in thermoelectric materials research: Looking back and moving forward. *Science* **2017,** *357* (6358), eaak9997.
5. Heremans, J. P.; Jovovic, V.; Toberer, E. S.; Saramat, A.; Kurosaki, K.; Charoenphakdee, A.; Yamanaka, S.; Snyder, G. J., Enhancement of Thermoelectric Efficiency in PbTe by Distortion of the Electronic Density of States. *Science* **2008,** *321* (5888), 554.
6. Zeier, W. G.; Zevalkink, A.; Gibbs, Z. M.; Hautier, G.; Kanatzidis, M. G.; Snyder, G. J., Thinking Like a Chemist: Intuition in Thermoelectric Materials. *Angew. Chem. Int. Ed.* **2016,** *55* (24), 6826-41.
7. Lee, J. K.; Son, J. H.; Kim, Y.-I.; Ryu, B.; Cho, B. J.; Kim, S.; Park, S.-D.; Oh, M.-W., Control of Carrier Concentration by Ag Doping in N-Type Bi2Te3 Based Compounds. *Appl. Sci.* **2018,** *8* (5), 735.
8. Kim, S. I.; Lee, K. H.; Mun, H. A.; Kim, H. S.; Hwang, S. W.; Roh, J. W.; Yang, D. J.; Shin, W. H.; Li, X. S.; Lee, Y. H.; Snyder, G. J.; Kim, S. W., Dense dislocation arrays embedded in grain boundaries for high-performance bulk thermoelectrics. *Science* **2015,** *348* (6230), 109.
9. Pan, Y.; Qiu, Y.; Witting, I.; Zhang, L.; Fu, C.; Li, J.-W.; Huang, Y.; Sun, F.-H.; He, J.; Snyder, G. J.; Felser, C.; Li, J.-F., Synergistic modulation of mobility and thermal conductivity in (Bi,Sb)2Te3 towards high thermoelectric performance. *Energy Environ. Sci.* **2019,** *12* (2), 624-630.
10. Meroz, O.; Ben-Ayoun, D.; Beeri, O.; Gelbstein, Y., Development of Bi2Te2.4Se0.6 alloy for thermoelectric power generation applications. *J. Alloys Compd.* **2016,** *679*, 196-201.
11. Meroz, O.; Gelbstein, Y., Thermoelectric Bi2Te3−xSex alloys for efficient thermal to electrical energy conversion. *Phys. Chem. Chem. Phys.* **2018,** *20* (6), 4092-4099.
12. Tsai, Y.-F.; Wei, P.-C.; Chang, L.; Wang, K.-K.; Yang, C.-C.; Lai, Y.-C.; Hsing, C.-R.; Wei, C.-M.; He, J.; Snyder, G. J.; Wu, H.-J., Compositional Fluctuations Locked by Athermal Transformation Yielding High Thermoelectric Performance in GeTe. *Adv. Mater.* **2021,** *33* (1), 2005612.
13. Lee, H. S.; Kim, B.-S.; Cho, C.-W.; Oh, M.-W.; Min, B.-K.; Park, S.-D.; Lee, H.-W., Herringbone structure in GeTe-based thermoelectric materials. *Acta Mater.* **2015,** *91*, 83-90.
14. Liu, Z. H.; Gao, W. H.; Zhang, W. H.; Sato, N.; Guo, Q. S.; Mori, T., High Power Factor and Enhanced Thermoelectric Performance in Sc and Bi Codoped GeTe: Insights into the Hidden Role of Rhombohedral Distortion Degree. *Adv. Energy Mater.* **2020,** *10* (42), 2002588.
15. Madar, N.; Givon, T.; Mogilyansky, D.; Gelbstein, Y., High thermoelectric potential of Bi2Te3 alloyed GeTe-rich phases. *J. Appl. Phys.* **2016,** *120* (3), 035102.
16. Dado, B.; Gelbstein, Y.; Dariel, M. P., Nucleation of nanosize particles following the spinodal decomposition in the pseudo-ternary Ge0.6Sn0.1Pb0.3Te compound. *Script. Mater.* **2010,** *62* (2), 89-92.
17. Sadia, Y.; Ohaion-Raz, T.; Ben-Yehuda, O.; Korngold, M.; Gelbstein, Y., Criteria for extending the operation periods of thermoelectric converters based on IV-VI compounds. *J. Solid State Chem.* **2016,** *241*, 79-85.
18. Ben-Ayoun, D.; Sadia, Y.; Gelbstein, Y., High temperature thermoelectric properties evolution of Pb1-xSnxTe based alloys. *J. Alloys Compd.* **2017,** *722*, 33-38.
19. Biswas, K.; He, J.; Blum, I. D.; Wu, C. I.; Hogan, T. P.; Seidman, D. N.; Dravid, V. P.; Kanatzidis, M. G., High-performance bulk thermoelectrics with all-scale hierarchical architectures. *Nature* **2012,** *489* (7416), 414-8.
20. Jang, H.; Park, J. H.; Lee, H. S.; Ryu, B.; Park, S. D.; Ju, H. A.; Yang, S. H.; Kim, Y. M.; Nam, W. H.; Wang, H.; Male, J.; Snyder, G. J.; Kim, M.; Jung, Y. S.; Oh, M. W., Regulating Te Vacancies through Dopant Balancing via Excess Ag Enables Rebounding Power Factor and High

Thermoelectric Performance in p-Type PbTe. *Adv. Sci.* **2021,** *8* (20), e2100895.
21. Zhao, L. D.; Lo, S. H.; Zhang, Y.; Sun, H.; Tan, G.; Uher, C.; Wolverton, C.; Dravid, V. P.; Kanatzidis, M. G., Ultralow thermal conductivity and high thermoelectric figure of merit in SnSe crystals. *Nature* **2014,** *508* (7496), 373-7.
22. Chang, C.; Wu, M.; He, D.; Pei, Y.; Wu, C. F.; Wu, X.; Yu, H.; Zhu, F.; Wang, K.; Chen, Y.; Huang, L.; Li, J. F.; He, J.; Zhao, L. D., 3D charge and 2D phonon transports leading to high out-of-plane ZT in n-type SnSe crystals. *Science* **2018,** *360* (6390), 778-783.
23. Zhao, L. D.; Tan, G.; Hao, S.; He, J.; Pei, Y.; Chi, H.; Wang, H.; Gong, S.; Xu, H.; Dravid, V. P.; Uher, C.; Snyder, G. J.; Wolverton, C.; Kanatzidis, M. G., Ultrahigh power factor and thermoelectric performance in hole-doped single-crystal SnSe. *Science* **2016,** *351* (6269), 141-4.
24. Lee, Y. K.; Luo, Z.; Cho, S. P.; Kanatzidis, M. G.; Chung, I., Surface Oxide Removal for Polycrystalline SnSe Reveals Near-Single-Crystal Thermoelectric Performance. *Joule* **2019,** *3* (3), 719-731.
25. Zhu, H.; Zhao, T.; Zhang, B.; An, Z.; Mao, S.; Wang, G.; Han, X.; Lu, X.; Zhang, J.; Zhou, X., Entropy Engineered Cubic n-Type AgBiSe2 Alloy with High Thermoelectric Performance in Fully Extended Operating Temperature Range. *Adv. Energy Mater.* **2020,** *11* (5), 2003304.
26. Pan, L.; Berardan, D.; Dragoe, N., High thermoelectric properties of n-type AgBiSe2. *J. Am. Chem. Soc.* **2013,** *135* (13), 4914-7.
27. Jang, H.; Abbey, S.; Nam, W. H.; Frimpong, B.; Nguyen, C. V.; Joo, S.-J.; Shin, H. S.; Song, J. Y.; Cho, E. N.; Kim, M.; Jung, Y. S.; Oh, M.-W., Order-disorder transition-induced band nestification in AgBiSe2–CuBiSe2 solid solutions for superior thermoelectric performance. *J. Mater. Chem. A* **2021,** *9* (8), 4648-4657.
28. Ohno, S.; Imasato, K.; Anand, S.; Tamaki, H.; Kang, S. D.; Gorai, P.; Sato, H. K.; Toberer, E. S.; Kanno, T.; Snyder, G. J., Phase Boundary Mapping to Obtain n-type Mg3Sb2-Based Thermoelectrics. *Joule* **2018,** *2* (1), 141-154.
29. Pan, Y.; Yao, M.; Hong, X.; Zhu, Y.; Fan, F.; Imasato, K.; He, Y.; Hess, C.; Fink, J.; Yang, J.; Büchner, B.; Fu, C.; Snyder, G. J.; Felser, C., Mg3(Bi,Sb)2 single crystals towards high thermoelectric performance. *Energy Environ. Sci.* **2020,** *13* (6), 1717-1724.
30. Zilber, T.; Cohen, S.; Fuks, D.; Gelbstein, Y., TiNiSn half-Heusler crystals grown from metallic flux for thermoelectric applications. *J. Alloys Compd.* **2019,** *781*, 1132-1138.
31. Jung, C.; Dutta, B.; Dey, P.; Jeon, S.-j.; Han, S.; Lee, H.-M.; Park, J.-S.; Yi, S.-H.; Choi, P.-P., Tailoring nanostructured NbCoSn-based thermoelectric materials via crystallization of an amorphous precursor. *Nano Energy* **2021,** *80*, 105518.
32. Sadia, Y.; Madar, N.; Kaler, I.; Gelbstein, Y., Thermoelectric Properties of the Quasi-Binary MnSi1.73-FeSi2 System. *J. Electron. Mater.* **2015,** *44* (6), 1637-1643.
33. de Boor, J.; Gupta, S.; Kolb, H.; Dasgupta, T.; Müller, E., Thermoelectric transport and microstructure of optimized Mg2Si0.8Sn0.2. *J. Mater. Chem. C* **2015,** *3* (40), 10467-10475.
34. Ryu, B.; Choi, E.-A.; Park, S.; Chung, J.; de Boor, J.; Ziolkowski, P.; Müller, E.; Park, S., Native point defects and low p-doping efficiency in Mg2(Si,Sn) solid solutions: A hybrid-density functional study. *J. Alloys Compd.* **2021,** *853*, 157145.
35. Liu, W.; Tan, X.; Yin, K.; Liu, H.; Tang, X.; Shi, J.; Zhang, Q.; Uher, C., Convergence of conduction bands as a means of enhancing thermoelectric performance of n-type Mg2Si(1-x)Sn(x) solid solutions. *Phys. Rev. Lett.* **2012,** *108* (16), 166601.
36. Sadia, Y.; Elegrably, M.; Ben-Nun, O.; Marciano, Y.; Gelbstein, Y., Submicron Features in Higher Manganese Silicide. *J. Nanomater.* **2013,** *2013*, 701268.
37. Luo, Y. B.; Cai, S. T.; Hao, S. Q.; Pielnhofer, F.; Hadar, I.; Luo, Z. Z.; Xu, J. W.; Wolverton, C.; Dravid, V. P.; Pfitzner, A.; Yan, Q. Y.; Kanatzidis, M. G., High-Performance Thermoelectrics from Cellular Nanostructured Sb2Si2Te6. *Joule* **2020,** *4* (1), 159-175.
38. Li, P.; Yu, J. Y.; Xu, J. R.; Zhang, L.; Huang, K., First-Principles Prediction of a New Family of Layered Topological Insulators. *Adv. Quantum Technol.* **2019,** *2* (11), 1900033.
39. Shannon, R. D., Revised Effective Ionic-Radii and Systematic Studies of Interatomic Distances in Halides and Chalcogenides. *Acta Crystallogr.* **1976,** *32* (Sep1), 751-767.
40. Flores, E. M.; Moreira, M. L.; Piotrowski, M. J., Structural and Electronic Properties of Bulk ZnX (X = O, S, Se, Te), ZnF2, and ZnO/ZnF2: A DFT Investigation within PBE, PBE + U, and Hybrid HSE Functionals. *J. Phys. Chem. A* **2020,** *124* (19), 3778-3785.
41. Perdew, J. P.; Yang, W.; Burke, K.; Yang, Z.; Gross, E. K.; Scheffler, M.; Scuseria, G. E.; Henderson, T. M.; Zhang, I. Y.; Ruzsinszky, A.; Peng, H.; Sun, J.; Trushin, E.; Gorling, A., Understanding band gaps of solids in generalized Kohn-Sham theory. *Prov. Natl. Acad. Sci.* **2017,** *114* (11), 2801-2806.
42. Oh, M. W.; Gu, J. J.; Inui, H.; Oh, M. H.; Wee, D. M., Evaluation of anisotropic thermoelectric power of ReSi1.75. *Physica B* **2007,** *389* (2), 367-371.
43. Goldsmid, H. J.; Sharp, J. W., Estimation of the thermal band gap of a semiconductor from Seebeck measurements. *J. Electron. Mater.* **1999,** *28* (7), 869-872.
44. Imasato, K.; Kang, S. D.; Ohno, S.; Snyder, G. J., Band engineering in Mg3Sb2 by alloying with Mg3Bi2 for enhanced thermoelectric performance. *Mater. Horiz.* **2018,** *5* (1), 59-64.
45. Snyder, G. J.; Snyder, A. H.; Wood, M.; Gurunathan, R.; Snyder, B. H.; Niu, C., Weighted Mobility. *Adv. Mater.* **2020,** *32* (25), e2001537.
46. Mao, J.; Shuai, J.; Song, S.; Wu, Y.; Dally, R.; Zhou, J.; Liu, Z.; Sun, J.; Zhang, Q.; Dela Cruz, C.; Wilson, S.; Pei, Y.; Singh, D. J.; Chen, G.; Chu, C. W.; Ren, Z., Manipulation of ionized impurity scattering for achieving high thermoelectric performance in n-type Mg3Sb2-based materials. *Prov. Natl. Acad. Sci.* **2017,** *114* (40), 10548-10553.
47. Wood, M.; Kuo, J. J.; Imasato, K.; Snyder, G. J., Improvement of Low-Temperature zT in a Mg3 Sb2 -Mg3 Bi2 Solid Solution via Mg-Vapor Annealing. *Adv. Mater.* **2019,** *31* (35), e1902337.

48. Imasato, K.; Fu, C.; Pan, Y.; Wood, M.; Kuo, J. J.; Felser, C.; Snyder, G. J., Metallic n-Type Mg3 Sb2 Single Crystals Demonstrate the Absence of Ionized Impurity Scattering and Enhanced Thermoelectric Performance. *Adv. Mater.* **2020,** *32* (16), e1908218.
49. Slade, T. J.; Grovogui, J. A.; Kuo, J. J.; Anand, S.; Bailey, T. P.; Wood, M.; Uher, C.; Snyder, G. J.; Dravid, V. P.; Kanatzidis, M. G., Understanding the thermally activated charge transport in NaPbmSbQm+2 (Q = S, Se, Te) thermoelectrics: weak dielectric screening leads to grain boundary dominated charge carrier scattering. *Energy Environ. Sci.* **2020,** *13* (5), 1509-1518.
50. Toberer, E. S.; Zevalkink, A.; Snyder, G. J., Phonon engineering through crystal chemistry. *J. Mater. Chem.* **2011,** *21* (40), 15843-15852.
51. Scanlon, D. O.; King, P. D. C.; Singh, R. P.; de la Torre, A.; Walker, S. M.; Balakrishnan, G.; Baumberger, F.; Catlow, C. R. A., Controlling Bulk Conductivity in Topological Insulators: Key Role of Anti-Site Defects. *Adv. Mater.* **2012,** *24* (16), 2154-2158.
52. Witting, I. T.; Chasapis, T. C.; Ricci, F.; Peters, M.; Heinz, N. A.; Hautier, G.; Snyder, G. J., The Thermoelectric Properties of Bismuth Telluride. *Adv. Electron. Mater.* **2019,** *5* (6), 1800904.
53. Jiang, Y.; Sun, Y. Y.; Chen, M.; Wang, Y.; Li, Z.; Song, C.; He, K.; Wang, L.; Chen, X.; Xue, Q. K.; Ma, X.; Zhang, S. B., Fermi-level tuning of epitaxial Sb2Te3 thin films on graphene by regulating intrinsic defects and substrate transfer doping. *Phys. Rev. Lett.* **2012,** *108* (6), 066809.
54. Ko, D. K.; Kang, Y.; Murray, C. B., Enhanced thermopower via carrier energy filtering in solution-processable Pt-Sb2Te3 nanocomposites. *Nano Lett.* **2011,** *11* (7), 2841-4.
55. Biswas, K.; He, J.; Zhang, Q.; Wang, G.; Uher, C.; Dravid, V. P.; Kanatzidis, M. G., Strained endotaxial nanostructures with high thermoelectric figure of merit. *Nat. Chem.* **2011,** *3* (2), 160-6.
56. Zhao, L. D.; He, J.; Hao, S.; Wu, C. I.; Hogan, T. P.; Wolverton, C.; Dravid, V. P.; Kanatzidis, M. G., Raising the thermoelectric performance of p-type PbS with endotaxial nanostructuring and valence-band offset engineering using CdS and ZnS. *J. Am. Chem. Soc.* **2012,** *134* (39), 16327-16336.
57. Yamasaka, S.; Watanabe, K.; Sakane, S.; Takeuchi, S.; Sakai, A.; Sawano, K.; Nakamura, Y., Independent control of electrical and heat conduction by nanostructure designing for Si-based thermoelectric materials. *Sci. Rep.* **2016,** *6* (1), 22838.
58. Shin, W. H.; Roh, J. W.; Ryu, B.; Chang, H. J.; Kim, H. S.; Lee, S.; Seo, W. S.; Ahn, K., Enhancing Thermoelectric Performances of Bismuth Antimony Telluride via Synergistic Combination of Multiscale Structuring and Band Alignment by FeTe2 Incorporation. *ACS Appl. Mater. Interfaces* **2018,** *10* (4), 3689-3698.
59. Xiao, Y.; Wang, D.; Zhang, Y.; Chen, C.; Zhang, S.; Wang, K.; Wang, G.; Pennycook, S. J.; Snyder, G. J.; Wu, H.; Zhao, L. D., Band Sharpening and Band Alignment Enable High Quality Factor to Enhance Thermoelectric Performance in n-Type PbS. *J. Am. Chem. Soc.* **2020,** *142* (8), 4051-4060.
60. Zhang, X.; Bu, Z.; Shi, X.; Chen, Z.; Lin, S.; Shan, B.; Wood, M.; Snyder, A. H.; Chen, L.; Snyder, G. J.; Pei, Y., Electronic quality factor for thermoelectrics. *Sci. Adv.* **2020,** *6* (46), eabc0726.
61. Ahmad, M.; Kodan, N.; Ghosh, A.; Mehta, B. R., The nature of 2D:3D SnS:Bi2Te3 interface and its effect on enhanced electrical and thermoelectric properties. *J. Alloys Compd.* **2020,** *847*, 156233.
62. Kumar, S.; Chaudhary, D.; Dhawan, P. K.; Yadav, R. R.; Khare, N., Bi2Te3-MWCNT nanocomposite: An efficient thermoelectric material. *Ceram. Int.* **2017,** *43* (17), 14976-14982.
63. Peng, L. P.; Liu, Z. T., Enhancing thermoelectric properties by using a surface polarization effect based on PEDOT:PSS thin films. *J. Mater. Chem. C* **2019,** *7* (20), 6120-6128.
64. Ahmad, M.; Varandani, D.; Mehta, B. R., Large surface charge accumulation in 2D MoS2/Sb2Te3 junction and its effect on junction properties: KPFM based study. *Appl. Phys. Lett.* **2018,** *113* (14), 141603.
65. Ziolkowski, P.; Karpinski, G.; Platzek, D.; Stiewe, C.; Muller, E. In *Application Overview of the Potential Seebeck Microscope*, 2006 25th International Conference on Thermoelectrics, 6-10 Aug. 2006; 2006; pp 684-688.
66. Ziolkowski, P.; Stiewe, C.; de Boor, J.; Druschke, I.; Zabrocki, K.; Edler, F.; Haupt, S.; Konig, J.; Mueller, E., Iron Disilicide as High-Temperature Reference Material for Traceable Measurements of Seebeck Coefficient Between 300 K and 800 K. *J. Electron. Mater.* **2017,** *46* (1), 51-63.
67. Ziolkowski, P.; Karpinski, G.; Dasgupta, T.; Muller, E., Probing thermopower on the microscale. *Phys. Status Solidi A* **2013,** *210* (1), 89-105.

Table of Contents (TOC) graphic